## Materials & Methods

### Cloning, protein expression and purification

The full-length protein of DeCLIC contains 642 residues, where the N-terminal 32 residues are predicted to be a signal peptide as shown by the SignalP 4.1 Server. The DeCLIC gene coding for the residues 33 to 642 was codon-optimized and chemically synthesized. The N-terminus of this DeCLIC construct was fused with a thrombin protease cleavage site followed by an MBP tag. The recombinant gene was sub-cloned into the pET20b vectors. The plasmids containing the recombinant gene were transfected into *E. coli* C43 competent cells strain and the protein was expressed in the 2YT medium. 1 mM ampicillin was present during the culture. When the OD had reached 0.3-0.4, the temperature was lowered to 20°C until the OD reaches 0.6-0.8 and 0.1 mM isopropyl β-D-1-thiogalactopyranoside (IPTG) was added for overnight induction. The culture was harvested and the cell pellet was suspended using buffer A that contains 20 mM Tris pH 8.0, 300 mM NaCl supplemented with EDTA-free protease inhibitor (ThermoFisher) and Benzonase nuclease. The mixture was disrupted by sonication and spun at 40,000 rpm for 1 h. The pellet containing the membrane was collected and was solubilized using buffer A supplemented with 4% n-dodecyl-β-D-maltoside (DDM) at 4°C for 3 h. The solubilized membrane was then spun at 28,000 rpm for 1 h and the supernatant was then incubated with an amylose resin (New England BioLabs) pre-equilibrated with buffer A, for half an hour. The amylose resin was then extensively washed by buffer A containing 0.1% DDM followed by buffer A containing 0.02% DDM. Buffer A containing 0.02% DDM and 50 mM D-(+)-maltose monohydrate (Sigma) was used to elute the recombinant protein. The recombinant protein was then concentrated and was applied to a pre-equilibrated Superose™ 6 Increase 10/300 GL (GE Healthcare) gel filtration column. Fractions from the elution peak corresponding to a molecular weight of five times MBP-DeCLIC were pooled. The MBP tag was removed by incubating the recombinant protein with the thrombin protease overnight. An additional round of size exclusive chromatography was applied to remove the MBP and thrombin. The peak corresponding to a molecular weight of five times DeCLIC was collected and concentrated to 10 mg/ml. All the purification steps were performed at 4°C. The concentrated DeCLIC protein was frozen using liquid nitrogen and was stored at -80°C for further use.

For the NTD1 construct, the DNA fragment of DeCLIC (34-202) was amplified from the synthesized full-length gene using the following primers:

Forward primer:

5'-CGTCGAGGATCCACGGAAGGTCGTGTACAGCATTTCACCGGA-3'

Reverse primer:

5'-CGAGCGGCCGCTTATTCCGGTTTGATTTCCAGGCTTGCCAG-3'.

The gene construct was sub-cloned into pRSFDuet vector with its N-terminal fused with a TEV cleavage site followed by a 14-histidine tag. The plasmids were transformed into *E. coli* BL21 (DE3) Rosetta2 strain. The recombinant protein was cultured in the LB medium in the presence of 1 mM Kanamycin and was induced by adding 0.04 mM IPTG when the OD was around 0.8 and incubated at 20°C overnight. The recombinant protein was purified first by Ni-NTA Agarose resin; the 14-histidine tag was removed by incubation of the recombinant protein with TEV protease overnight. The protein was further purified by size exclusion chromatography using Superdex 200 Increase GL column. The purified protein was then concentrated to 15 mg/ml in the buffer containing 20 mM Tris pH 7.6, 150 mM NaCl. The purification steps were maintained at 4 °C. The purified protein was frozen with liquid nitrogen and was stored at -80°C. The Se-Met protein of DeCLIC 34-202 was purified using a similar protocol, except that 1 mM DTT was added during the purification step.

**Crystallization and data collection**

All the crystallization trials were performed at 18 °C using the hanging drop method. The crystals of $Ca^{2+}$-bound DeCLIC were obtained by mixing DeCLIC protein at 10 mg/ml with an equal volume of the reservoir solution containing 100 mM Tris pH 7.5, 250 mM $CaCl_2$, 14.5% (w/v) PEG-MME 2000 in a 1 µl:1 µl volume ratio. The final pH in the crystallization drop was around 6.7. Crystals started to appear after two days and grew to full size after one week. The crystals were cryo-protected with an additional 25% of ethylene glycol (v/v) before flash freezing in liquid nitrogen. The crystals of the complex with $Ba^{2+}$ were prepared by soaking the crystals with the mother liquor supplemented by 200 mM $BaCl_2$ for 5-10 minutes.

The open pore conformation crystals of DeCLIC were obtained by mixing the DeCLIC protein 10 mg/ml with an equal volume of the reservoir buffer containing 0.3 M NH4-Formate, 0.1 M Tris 7.5, 30% (v/v) PEG-MME 500 in a 1 µl : 1 µl volume ratio. The final pH in the crystallization drop was around 7.6. Crystals appeared overnight and grew to full size after approximately three weeks. The crystals were directly flash frozen in liquid nitrogen.

The NTD1 of DeCLIC (33-202 residues) was crystallized in conditions containing 0.1 M HEPES pH 6.5, 0.7 M $NaH_2PO_4$, 0.7 M $KH_2PO_4$. The same conditions were used to

prepare crystals of Se-Met NTD1-DeCLIC (34-202). The crystals were flash frozen with mother liquor supplemented with 30% glycerol (v/v).

In order to increase the quality and reproducibility of the crystals, the micro-seeding procedure was applied after setting up crystallization. Diffraction data sets were collected at Soleil PROXIMA-1 and were processed using XDS[1] and CCP4[2] software. The closed form crystals belong to $P2_12_12$ space group with one pentamer in the asymmetric unit. The open form crystals belong to $P2_1$ space group with one pentamer in the asymmetric unit. The N-terminal 34-202 segment crystallized in $P6_1$ space group with two molecules in the asymmetric unit. Data collection statistics are reported in **Table S1**.

**Structure determination and model refinement**

Initial phases of the DeCLIC NTD1 domain alone were obtained using PHENIX[3] from single anomalous diffraction (SAD) data set collected at 0.9791 Å wavelength. The initial model was generated through AutoBuild in PHENIX. Multiple rounds of model building in Coot[4] and refinement with BUSTER[5] were performed to obtain the final refined model of DeCLIC NTD1 containing residues 33-195.

The initial phases of $Ca^{2+}$-bound DeCLIC were solved by molecular replacement using a chimera model containing the ECD of GLIC (PDB ID: 4HFI)[6] and the TMD of ELIC (PDB ID: 2VL0)[7] as a search model through PHASER in Phenix[8]. The refinement was performed using Refmac[2] and BUSTER-Refine[5] by alternating cycles of refinement and manual building in Coot[4]. The electron density became visible in the NTDs after building most parts of LBD and TMD. The NTD2 (200-320) was built by taking advantage of the structural information of 3JQW, whose structure was predicted by the HHpred website[9] to share a fold similar to both NTD1 and NTD2 domains. The NTD1 model from the crystallized segment of 33-195 (see below) was manually fitted into the density, followed by the rigid body refinement, and finally adjusted/re-built into the density using Coot. During the refinement, automatic non-crystallographic symmetry (NCS) restraints were applied.

The phase problem of the open pore form structure was solved by molecular replacement using sTeLIC as a search model, whose structure has been captured in its widely open pore conformation[22]. Before molecular replacement, the structural model of sTeLIC was trimmed by the program Chainsaw in CCP4[11]. During the refinement, NCS restraints were applied. Further refinement was carried out using the Refmac[2] and BUSTER[5] refinement programs. We also collected one data set at the mercury edge wavelength for the open form crystals co-crystalized with 10 mM ethylmercury chloride ($C_2H_5HgCl$). There are 6 cysteines

in each DeCLIC monomer: two are located in NTD2 and form one disulfide bridge; two are located in the LBD and also form a disulfide bridge; the remaining two are located in the M3 helix. The overall limited resolution as well as the relatively weak anomalous signal coming from a single mercury atom bound were not enough to phase the whole receptor but helped to confirm the correct assignment of the sequence in the region of M3 (only C596 was found labeled with ethylmercury chloride) once the model was completed.

**Electrophysiology**

Two-electrode voltage-clamp electrophysiology was performed as previously described[12]. Briefly, cDNA encoding DeCLIC or ΔNTD variants was commercially synthesized (Thermo Fisher) and subcloned into the pUNIV oocyte vector[13]. Plasmids were linearized with NotI (Promega) and transcribed using the T7 mMESSAGE mMACHINE kit (Life Technologies, Austin, TX, USA). Extracted and isolated oocytes from female *Xenopus* laevis frogs were purchased from EcoCyte Bioscience (Castrop-Rauxel, Germany), stored in incubation medium (88 mM NaCl, 10 mM HEPES, 2.4 mM $NaHCO_3$, 1 mM KCl, 0.91 mM $CaCl_2$, 0.82 mM $MgSO_4$, 0.33 mM $Ca(NO_3)_2$, 2 mM sodium pyruvate, 0.5 mM theophylline, 0.1 mM gentamicin, 17 mM streptomycin, and 10 000 U/l penicillin, passed through a 0.22 μm filter and adjusted to pH 7.5), and injected with 30 ng RNA in 50.6 nL each using a Nanoject II microinjector (Drummond Scientific, Broomall, PA, USA) fitted with a borosilicate glass capillary with a 20–30 μm tip, pulled with a PC-10 Narishige Puller (Narishige Group, Tokyo, Japan). Injected oocytes were stored individually in incubation medium at 12°C for 1–3 weeks, or with 0.5 ng YFP RNA as an injection control.

For each recording, control, YFP- or DeCLIC-injected oocytes were clamped on either side of a parallel recording rig using an OC-725C amplifier (Warner Instruments, Hamden, CT, USA) and perfused at a flow rate of 0.5–1.0 mL/min in running buffer (10 mM Tris, 123 mM NaCl, 10 mM $Na^+$-citrate, 2 mM KCl, 2 mM $MgSO_4$, with varying concentrations of $CaCl_2$), adjusted to pH 8.5 to minimize background responses to $Ca^{2+}$ depletion. Glass electrodes were pulled and filled with 3 M KCl to reach an initial resistance of 8–80 MΩ. Currents were digitized at a sampling rate of 5 kHz with an Axon CNS 1440A Digidata system running pCLAMP 10 (Molecular Devices, Sunnyvale, CA, USA). For $Ca^{2+}$ sensitivity measurements, peak currents at each concentration were normalized to the maximal response of paired oocytes, and fit to a sigmoidal concentration-response curve using Prism8 (GraphPad, La Jolla, CA, USA).

**The torsional elastic network and the dynamical couplings.**

The dynamical couplings between atoms belonging to the same functional site and to different sites were computed as described by Alfayate et al.[14], adopting the normal modes of the TNM model[15], which do not deform the stereochemistry of the molecule even for high amplitudes movements. Namely, i) the directionality coupling is defined as the Boltzmann average of the scalar product between the directions of movement of the two atoms (it is related to the covariance but emphasizes small and precise movements that are common in functional sites), ii) the coordination coupling is defined as a constant minus the root mean square of the fluctuation of the distance between the two atoms so that atoms bound to a common ligand tend to have large coordination, and iii) the deformation coupling is defined as the deformation caused on an atom produced by a perturbation applied to the other atom with constant amplitude and direction such that the perturbation is maximized (this perturbation is related to the allosteric effect, it can be computed analytically using linear response theory and in this regime it is symmetric for the exchange of the two atoms). In **Fig. 7f** and **Fig. 7g** the predicted movement of the centre of mass is projected along the principal axes given by spectral decomposition of the inertia matrix, the projections are squared, and the Boltzmann averages are computed using the normal modes.

In order to test whether the couplings/profiles within and between sites are significantly larger than expected by chance, for each biological site constituted by residues $i_1 \cdots i_n$ we drew 1000 random sets of residues $j_1 \cdots j_n$ with the same distances in primary sequence as in the biological site, since this distance is a major determinant of the dynamical couplings. Specifically, we drew residue $j_1$ and chose the other ones as $j_k = j_1 + (i_k - i_1)$. Note that it is not guaranteed that these residues are close in space. Pairs of sites were constructed as if they constitute a single site. If a site or a pair of sites was distributed on two or more chains, each part in a different chain was drawn independently. We then computed the average and standard deviation of the couplings between these randomly generated sites and measured the Z-score from it.

As a test of the TNM calculations, the model predicted atomic fluctuations that correlate very well with the observed B factors (correlation factor of 0.94 for the closed and 0.88 for the open conformation, **Fig. S16a**) when the rigid body degrees of freedom are taken into account and the fit is regularized through rescaled ridge regression[16]. Here the force constant was set equal for the two conformations instead of fitting it from B-factors, and the

overall extent of the predicted fluctuations was almost equal. The contribution of normal modes to the conformational transition was calculated as described in Bastolla and Dehouck, 2019[14]. Only a handful of normal modes, mostly of low frequency, were necessary to explain 80% of the torsional part of the conformational change: 18 modes in the case of the open-to-closed transition (mode 4 alone explains 46% of the transition) and 59 modes for the closed-to-open transition, see **Fig. S16b**. As expected, the co-directionality coupling showed that neighbouring chains are always more correlated than second neighbours in both forms, as shown in **Fig. S16c**. In Figure **S16d** one can see that the atoms of the pore experience a qualitative change between the closed and the open conformation, from being more coordinated and co-directional and less deformable than expected by chance to the opposite situation. No other site exhibited the same qualitative change as the pore.

## References:


1. Kabsch, W. Integration, scaling, space-group assignment and post-refinement. *Acta Crystallogr. D Biol. Crystallogr.* **66**, 133–144 (2010).
2. Winn, M. D. *et al.* Overview of the CCP4 suite and current developments. *Acta Crystallogr. D Biol. Crystallogr.* **67**, 235–242 (2011).
3. Adams, P. D. *et al.* PHENIX: a comprehensive Python-based system for macromolecular structure solution. *Acta Crystallogr. D Biol. Crystallogr.* **66**, 213–221 (2010).
4. Emsley, P., Lohkamp, B., Scott, W. G. & Cowtan, K. Features and development of Coot. *Acta Crystallogr. D Biol. Crystallogr.* **66**, 486–501 (2010).
5. Blanc, E. *et al.* Refinement of severely incomplete structures with maximum likelihood in BUSTER-TNT. *Acta Crystallogr. D Biol. Crystallogr.* **60**, 2210–2221 (2004).
6. Sauguet, L. *et al.* Structural basis for ion permeation mechanism in pentameric ligand-gated ion channels. *EMBO J.* **32**, 728–741 (2013).
7. Bocquet, N. *et al.* A prokaryotic proton-gated ion channel from the nicotinic acetylcholine receptor family. *Nature* **445**, 116–119 (2007).
8. McCoy, A. J. *et al.* Phaser crystallographic software. *J. Appl. Crystallogr.* **40**, 658–674 (2007).
9. Söding, J., Biegert, A. & Lupas, A. N. The HHpred interactive server for protein homology detection and structure prediction. *Nucleic Acids Res.* **33**, W244–W248 (2005).
10. Hu, H. *et al.* Crystal structures of a pentameric ion channel gated by alkaline pH show a widely open pore and identify a cavity for modulation. *Proc. Natl. Acad. Sci. U. S. A.* **115**, E3959–E3968 (2018).
11. Stein, N. CHAINSAW: a program for mutating pdb files used as templates in molecular replacement. *J. Appl. Crystallogr.* **41**, 641–643 (2008).
12. Heusser, S. A. *et al.* Functional characterization of neurotransmitter activation and modulation in a nematode model ligand-gated ion channel. *J. Neurochem.* **138**, 243–253 (2016).
13. Venkatachalan, S. P. *et al.* Optimized expression vector for ion channel studies in Xenopus oocytes and mammalian cells using alfalfa mosaic virus. *Pflugers Arch.* **454**, 155 (2007).
14. Alfayate, A., Caceres, C. R., Gomes Dos Santos, H. & Bastolla, U. Predicted dynamical couplings of protein residues characterize catalysis, transport and allostery. *Bioinforma. Oxf. Engl.* (2019) doi:10.1093/bioinformatics/btz301.
15. Mendez, R. & Bastolla, U. Torsional network model: normal modes in torsion angle space better correlate with conformation changes in proteins. *Phys. Rev. Lett.* **104**, 228103 (2010).
16. Dehouck, Y. & Bastolla, U. The maximum penalty criterion for ridge regression: application to the calibration of the force constant in elastic network models. *Integr. Biol. Quant. Biosci. Nano Macro* **9**, 627–641 (2017).
17. Ashkenazy, H. *et al.* ConSurf 2016: an improved methodology to estimate and visualize evolutionary conservation in macromolecules. *Nucleic Acids Res.* **44**, W344–W350 (2016).
18. Ho, B. K. & Gruswitz, F. HOLLOW: generating accurate representations of channel and interior surfaces in molecular structures. *BMC Struct. Biol.* **8**, 49 (2008).

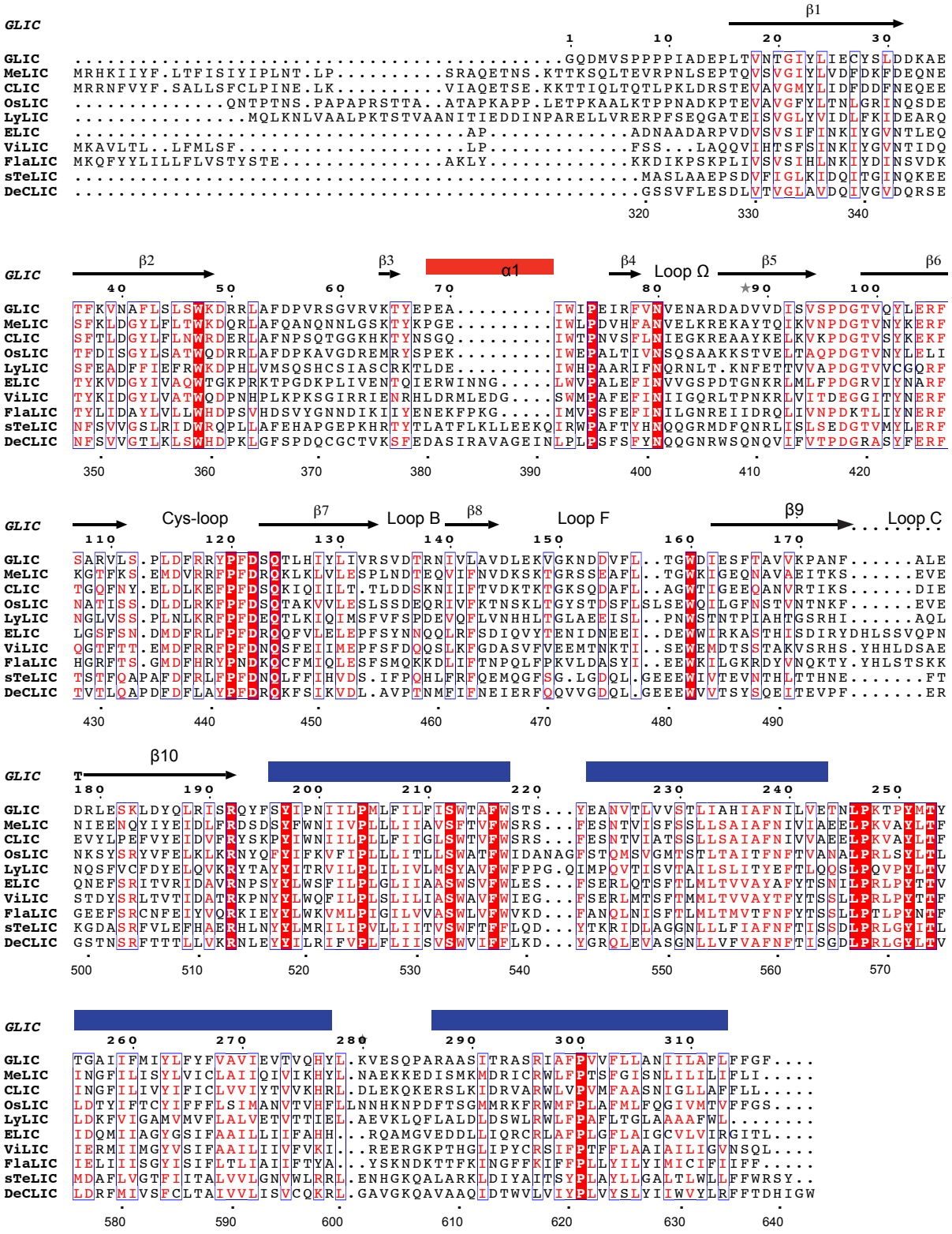


**Figure S1. Bacterial pLGICs with a known structure, and relatives.**
Sequence alignment of bacterial pLGIC receptors whose structure is known in at least one conformational state (Organism/Uniprot entry name): GLIC (Gloeobacter violaceus/Q7NDN8), ELIC (Dickeya chrysanthemi/P0C7B7), sTeLIC (endosymbiont of Tevnia jerichonana/G2FID1), DeCLIC (uncultured Desulfofustis sp. PB-SRB1/V4JF97). In addition, we added the four closest homologues of GLIC: MeLIC (Merismopedia glauca/A0A2T1C4Y5), CLIC (Chroococcidiopsis thermalis/K9U6Q3), OsLIC (Oscillatoria nigro-viridis/K9VN17), LyLIC (Lyngbya aestuarii/U7QEN5) and the 2 closest homologues of ELIC: ViLIC (Vibrio nigripulchritudo/U4EC21) and FlaLIC (Flavobacterium johnsoniae/A0A1M5UNA1) are shown.

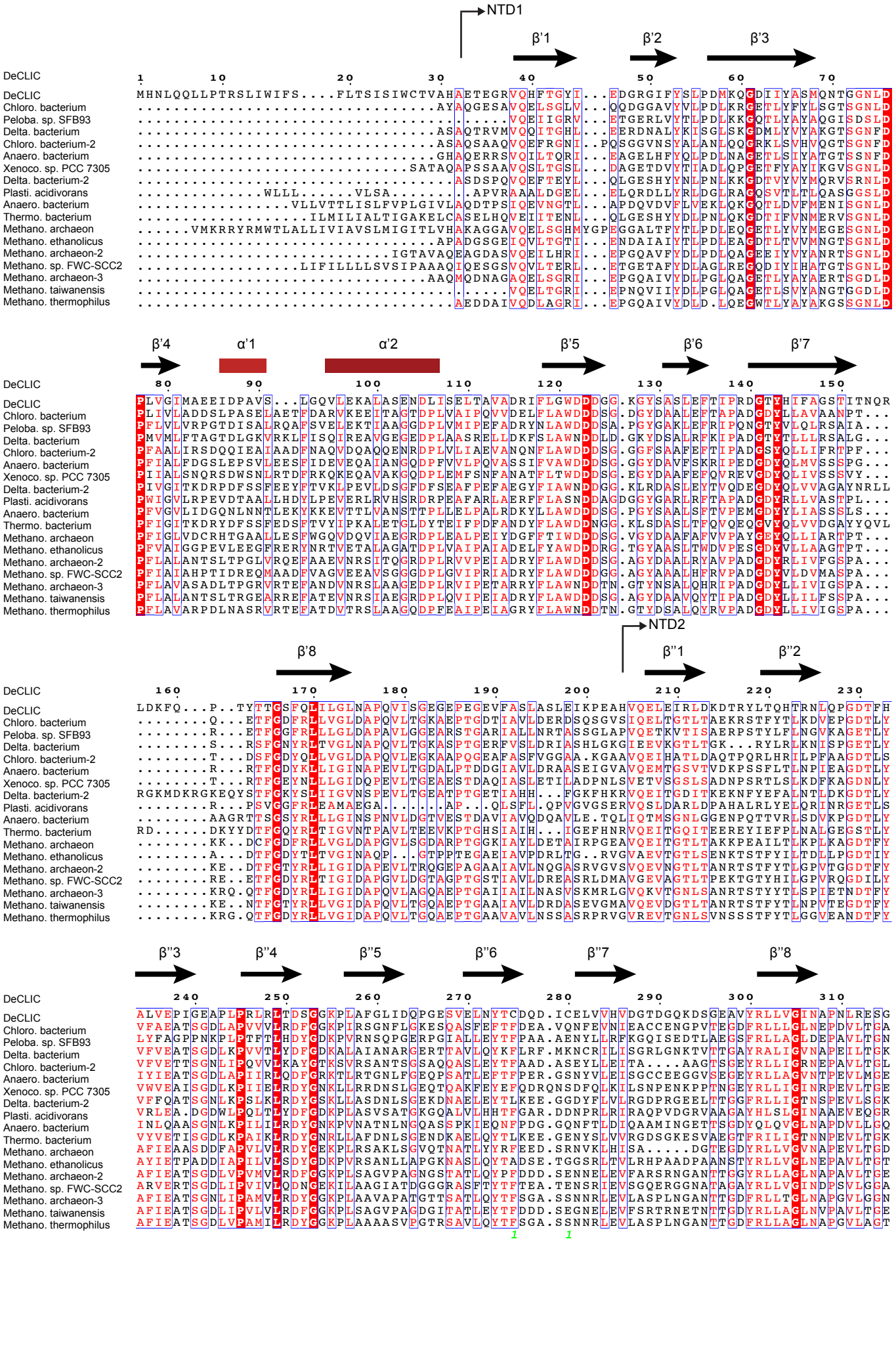
NTD1
β'1
β'2
β'3
DeCLIC
Chloro. bacterium
Peloba. sp. SFB93
Delta. bacterium
Chloro. bacterium-2
Anaero. bacterium
Xenoco. sp. PCC 7305
Delta. bacterium-2
Plasti. acidivorans
Anaero. bacterium
Thermo. bacterium
Methano. archaeon
Methano. ethanolicus
Methano. archaeon-2
Methano. sp. FWC-SCC2
Methano. archaeon-3
Methano. taiwanensis
Methano. thermophilus
β'4
α'1
α'2
β'5
β'6
β'7
NTD2
β"1
β"2
β'8
β"3
β"4
β"5
β"6
β"7
β"8

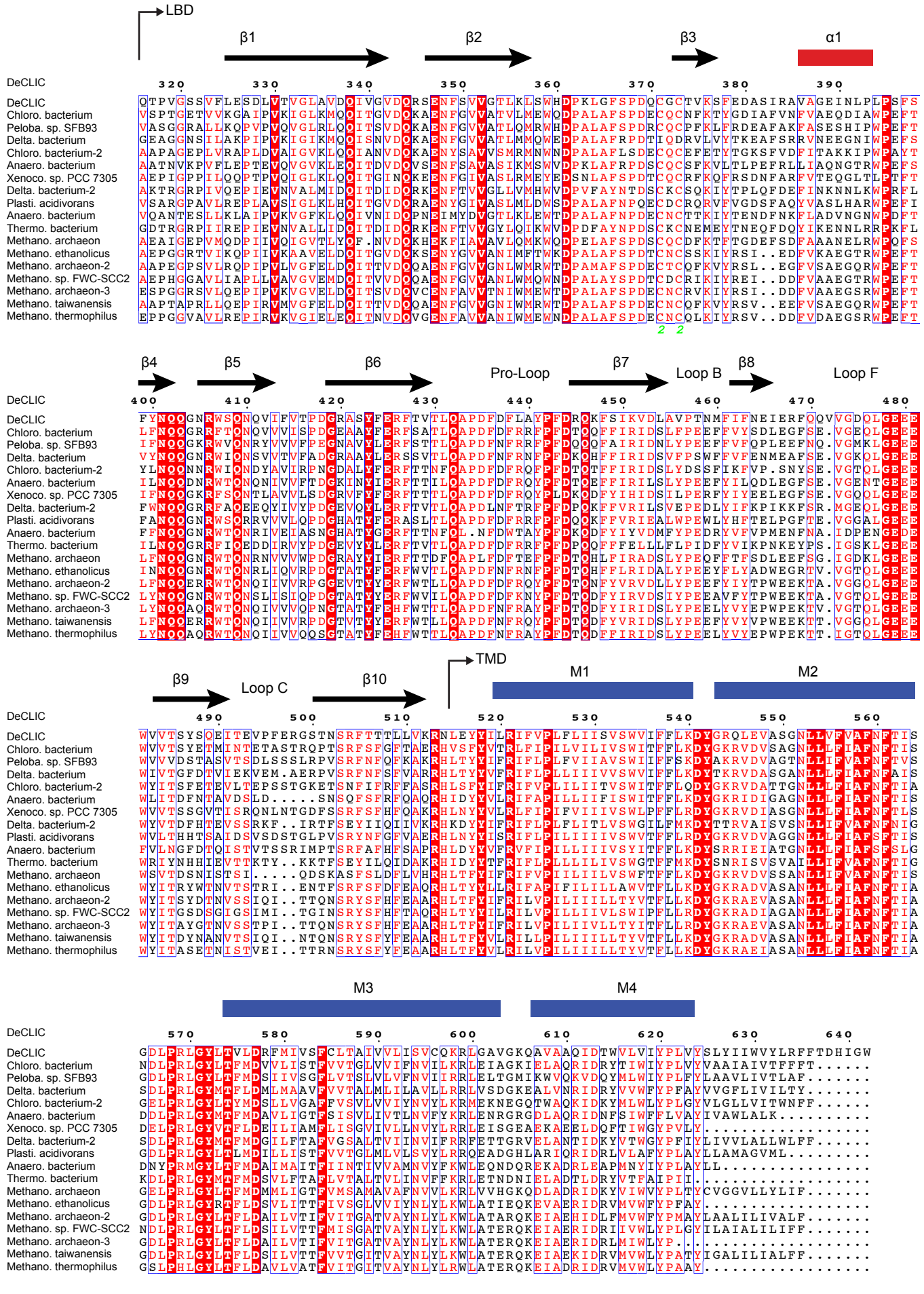
LBD
β1
β2
β3
α1
β4
β5
β6
Pro-Loop
β7
Loop B
β8
Loop F
β9
Loop C
β10
TMD
M1
M2
M3
M4
DeCLIC
Chloro. bacterium
Peloba. sp. SFB93
Delta. bacterium
Chloro. bacterium-2
Anaero. bacterium
Xenoco. sp. PCC 7305
Delta. bacterium-2
Plasti. acidivorans
Anaero. bacterium
Thermo. bacterium
Methano. archaeon
Methano. ethanolicus
Methano. archaeon-2
Methano. sp. FWC-SCC2
Methano. archaeon-3
Methano. taiwanensis
Methano. thermophilus

**Figure S2. Sequence of DeCLIC and related prokaryotic channels.**
Multiple sequence alignment of DeCLIC with its most closely related pLGICs, all containing the additional periplasmic two-lobed NTDs (Organism/Uniprot entry name or Gene bank ID): uncultured Desulfofustis sp. PB-SRB1/V4JF97; Chloroflexi bacterium/A0A3D0UJ23; Pelobacter sp. SFB93/WP_083553162; Deltaproteobacteria bacterium/A0A355EMH6; Chloroflexi bacterium-2/A0A359HMB9; Anaerolineales bacterium/A0A523TXT8; Xenococcus sp. PCC 7305/L8LWJ4; Deltaproteobacteria bacterium-2/A0A523JAG3; Plasticicumulans acidivorans/A0A317MXN3; Anaerolineales bacterium/A0A363T825; Thermodesulfobacteriales bacterium/A0A524JLX2; Methanophagales archaeon/A0A368TJA8; Methanofollis ethanolicus/WP_067049892.1; Methanomicrobiales archaeon HGW-Methanomicrobiales-2/A0A2I0PAI0; Methanofollis sp. FWC-SCC2/A0A483CWB6; Methanomicrobiales archaeon HGW-Methanomicrobiales-2/A0A2I0PA37; Methanoculleus taiwanensis/WP_128692492.1; Methanoculleus thermophiles/A0A1G8XSP6

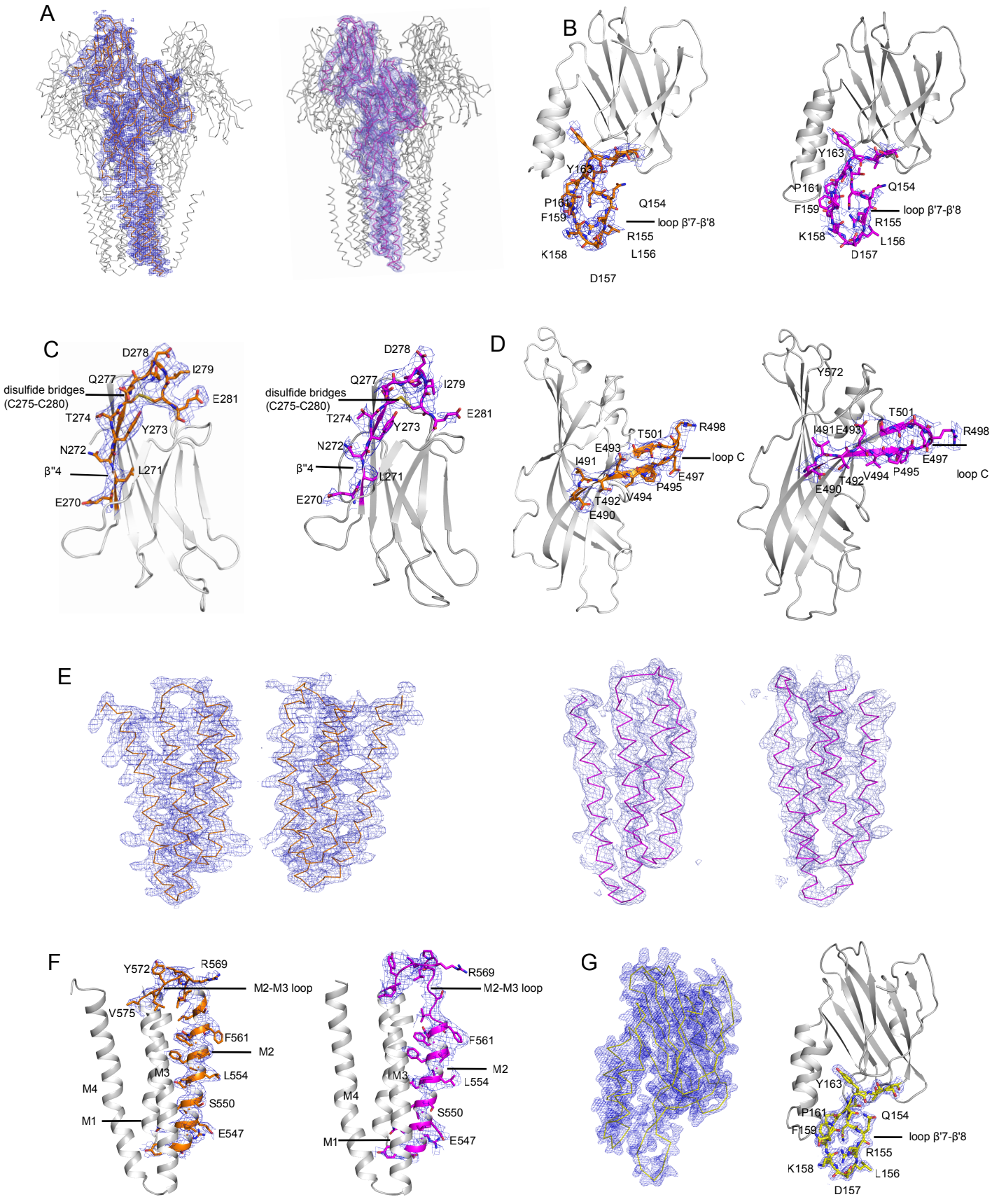


**Figure S3. Representative experimental electron densities of DeCLIC.**
Panels (A)-(F) depict 2Fo-Fc maps (blue mesh) contoured at 1.0 σ around equivalent regions of $Ca^{2+}$ bound (left) and $Ca^{2+}$ free (right) full-length DeCLIC structures, for (A) a single DeCLIC subunit; (B) β'7-β'8 loop of the NTD1 lobe; (C) β"4–β"5 loop of the NTD2 lobe; (D) loop C in the LBD; (E) transmembrane helices in two TMD subunits; (F) M2 helix and M2–M3 loop in the TMD. (G) Electron densities around the truncated DeCLIC-NTD1 structure alone.

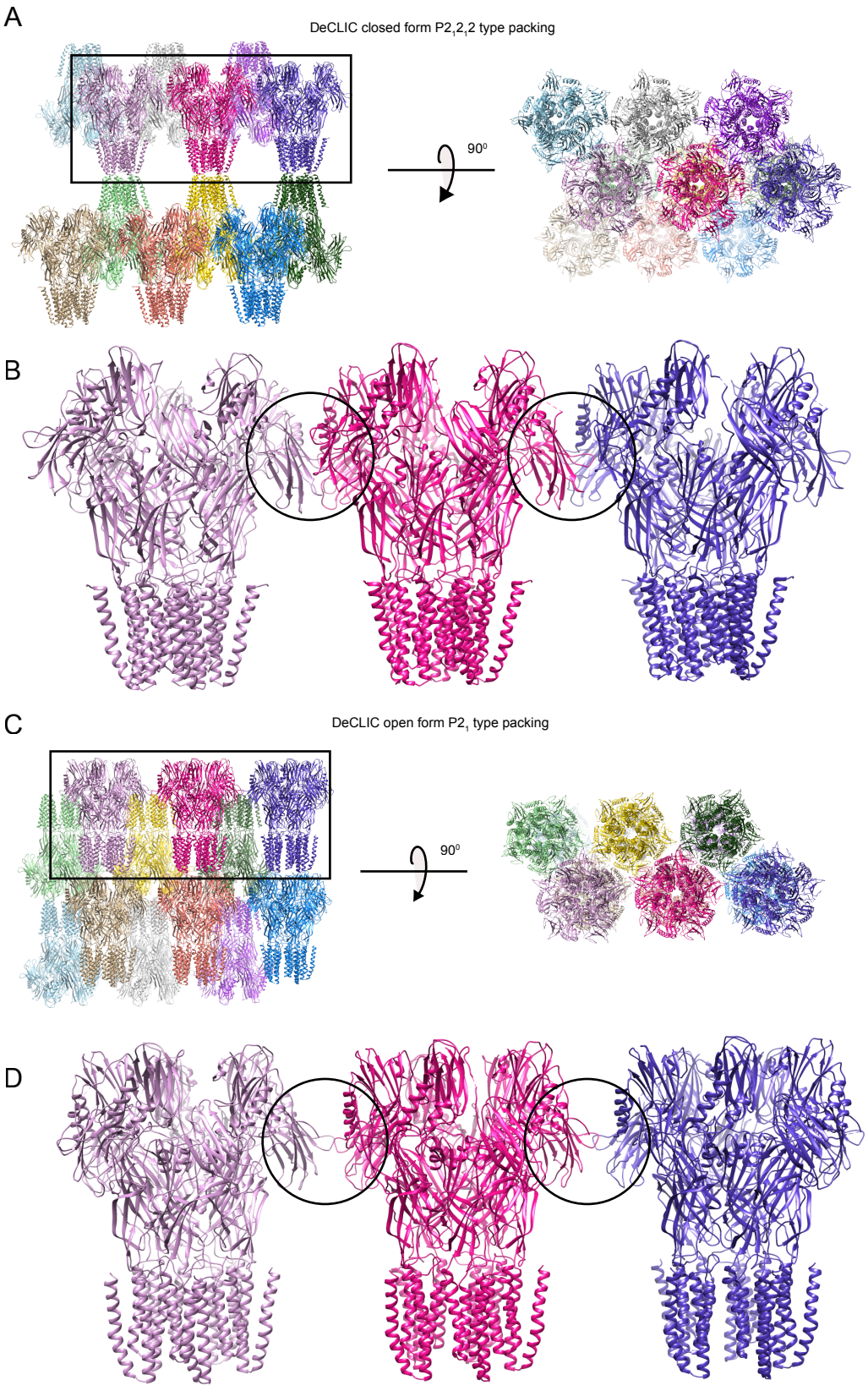


**Figure S4. Packing interactions of DeCLIC in its two crystal forms.**
(A) Packing of DeCLIC, colored by pentamer, in crystals grown in the presence of $Ca^{2+}$. (B) Detail view showing specific crystal contacts in the boxed region of *A*. (C) View as in a of crystals grown in the absence of $Ca^{2+}$. (D) Detail view for the boxed region of *C*.

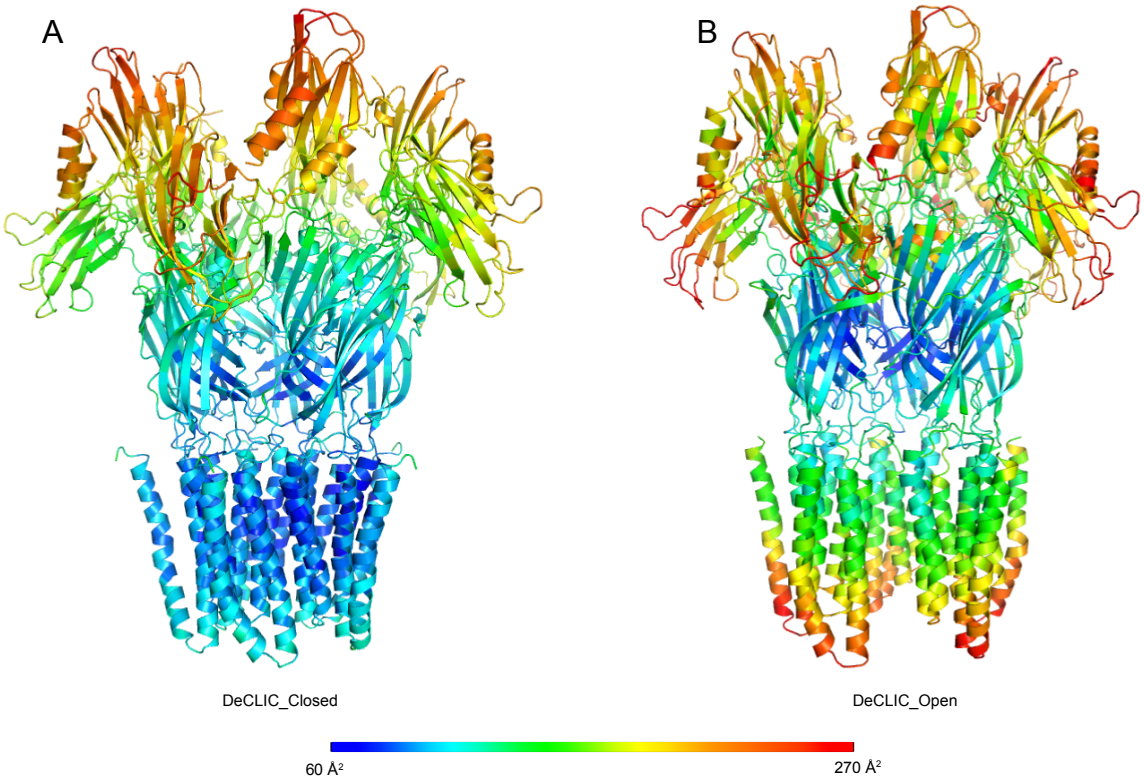


**Figure S5. Distribution of B-factors in the two conformations of DeCLIC.** (A) Ribbon representation of DeCLIC structure in the presence of $Ca^{2+}$, viewed from the membrane plane and colored by B-factor values according to the scale bar shown in the bottom. (B) View as in a of DeCLIC structure in the absence of $Ca^{2+}$.

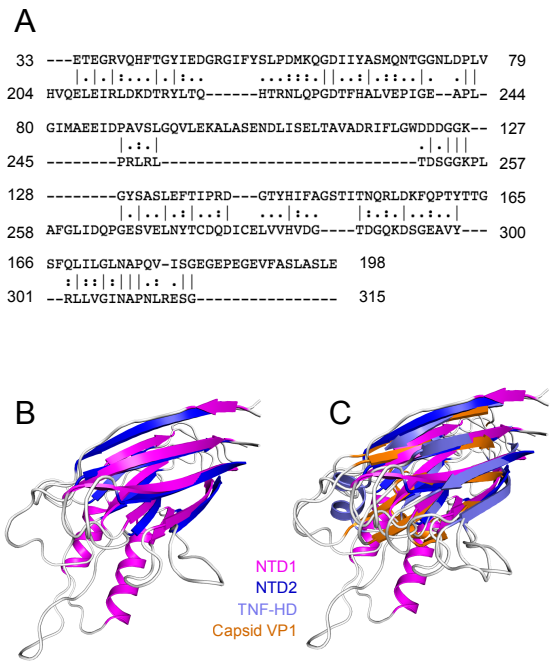


**Figure S6. Topologies and patterns of hydrophobicity in NTD1 and NTD2.**

(A) Sequence alignment of NTD1 with NDT2. (B) Superposition of NTD1 (magenta) and NTD2 (blue) from a single subunit, demonstrating their homologous jelly-roll folds. (C) Superposition as in *B* with a tumor necrosis factor homology domain (TNF-HD, light blue; PDB ID 2HEY) and human parechovirus capsid VP1 (orange; PDB ID 5M74).

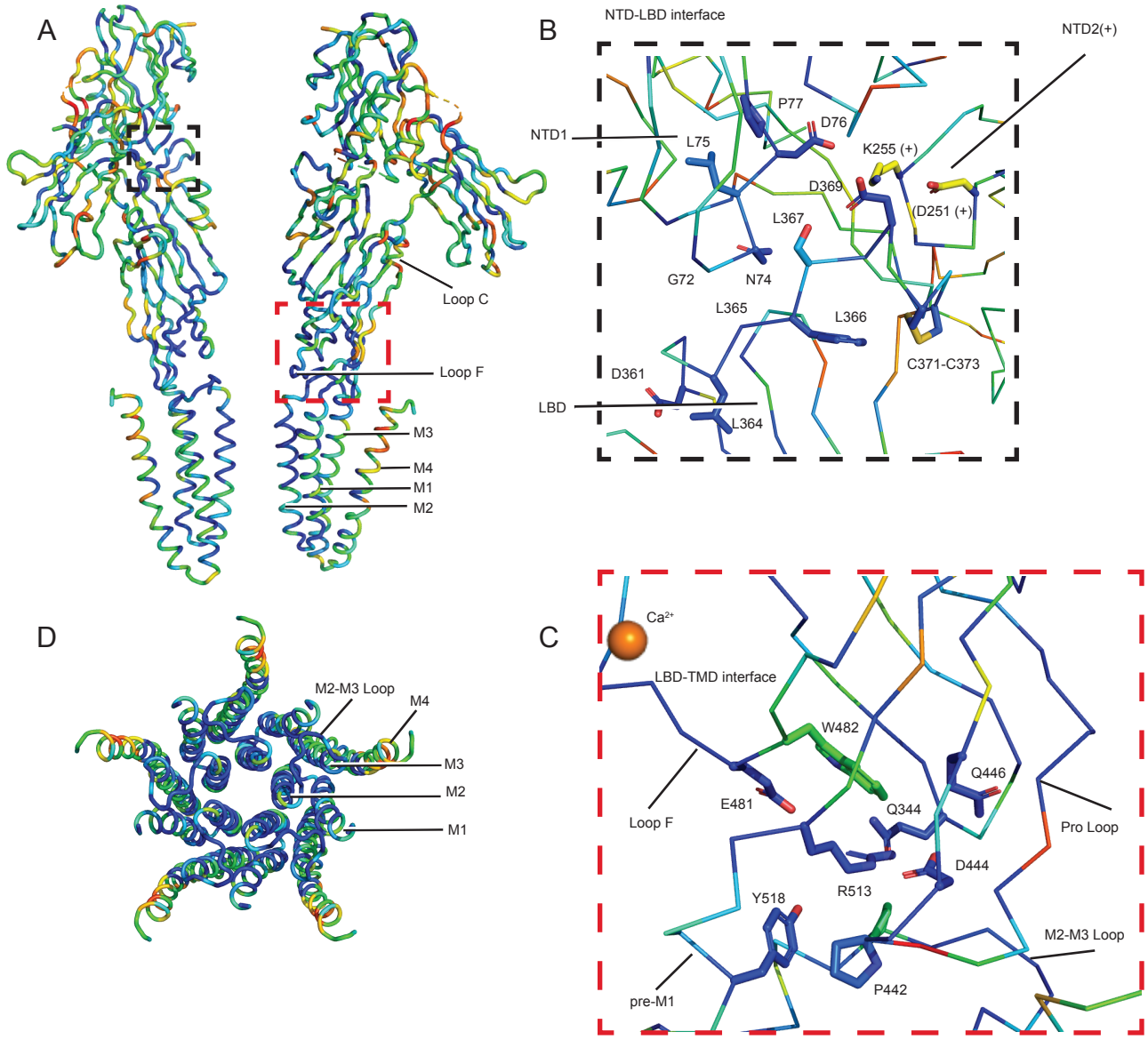


**Figure S7. Structural context of sequence conservation in DeCLIC homologues.** (A) DeCLIC structure in the presence of $Ca^{2+}$, viewed from the membrane plane; for clarity, only two subunits are shown. Residues are colored from most (blue) to least conserved (red) based on a multiple sequence alignment with its 18 closest homologs (Fig. S2), as calculated using the ConSurf Server17. (B) Detail view showing conserved NTD-LBD interface contacts in the black-boxed region of *A*. Residues from the complementary neighboring subunit are indicated (+). (C) Detail view of conserved LBD-TMD interface contacts in the green-boxed region of *A*. The Calcium binding site is shown as orange sphere. (D) Detail view of the DeCLIC TMD.

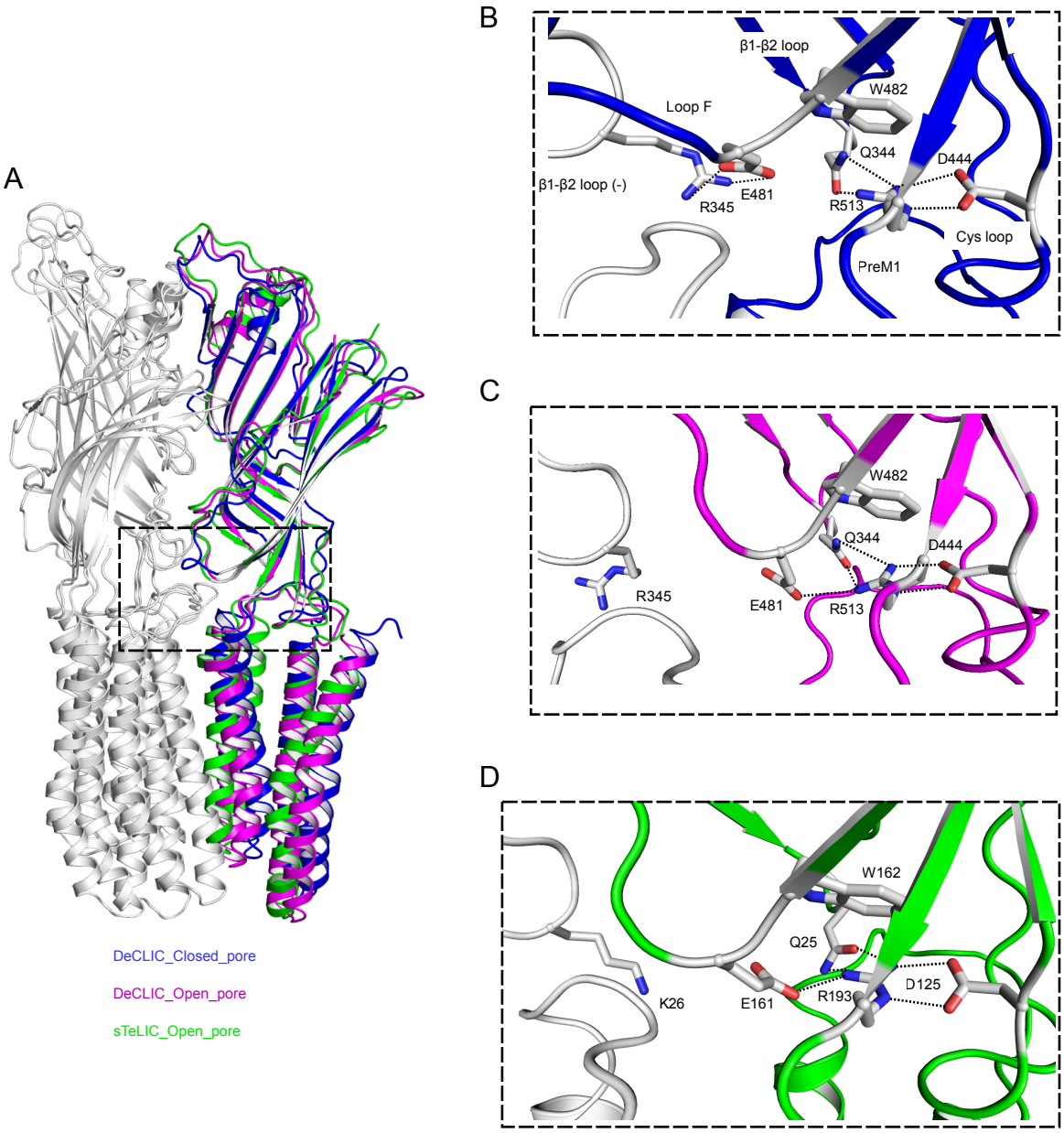


**Figure S8. Electrostatic interactions at the LBD-TMD interface.**
(A) Superposition of DeCLIC structures in the presence (blue) and absence (magenta) of $Ca^{2+}$ with that of sTeLIC (green), viewed from the membrane plane. For clarity, the DeCLIC NTD is hidden, and only two proximal subunits are shown. (B)-(D), Detail views of interfacial electrostatic contacts (salt bridges) in the boxed regions of *A* in $Ca^{2+}$ bound DeCLIC (B), $Ca^{2+}$ free DeCLIC (C) and sTeLIC (D).

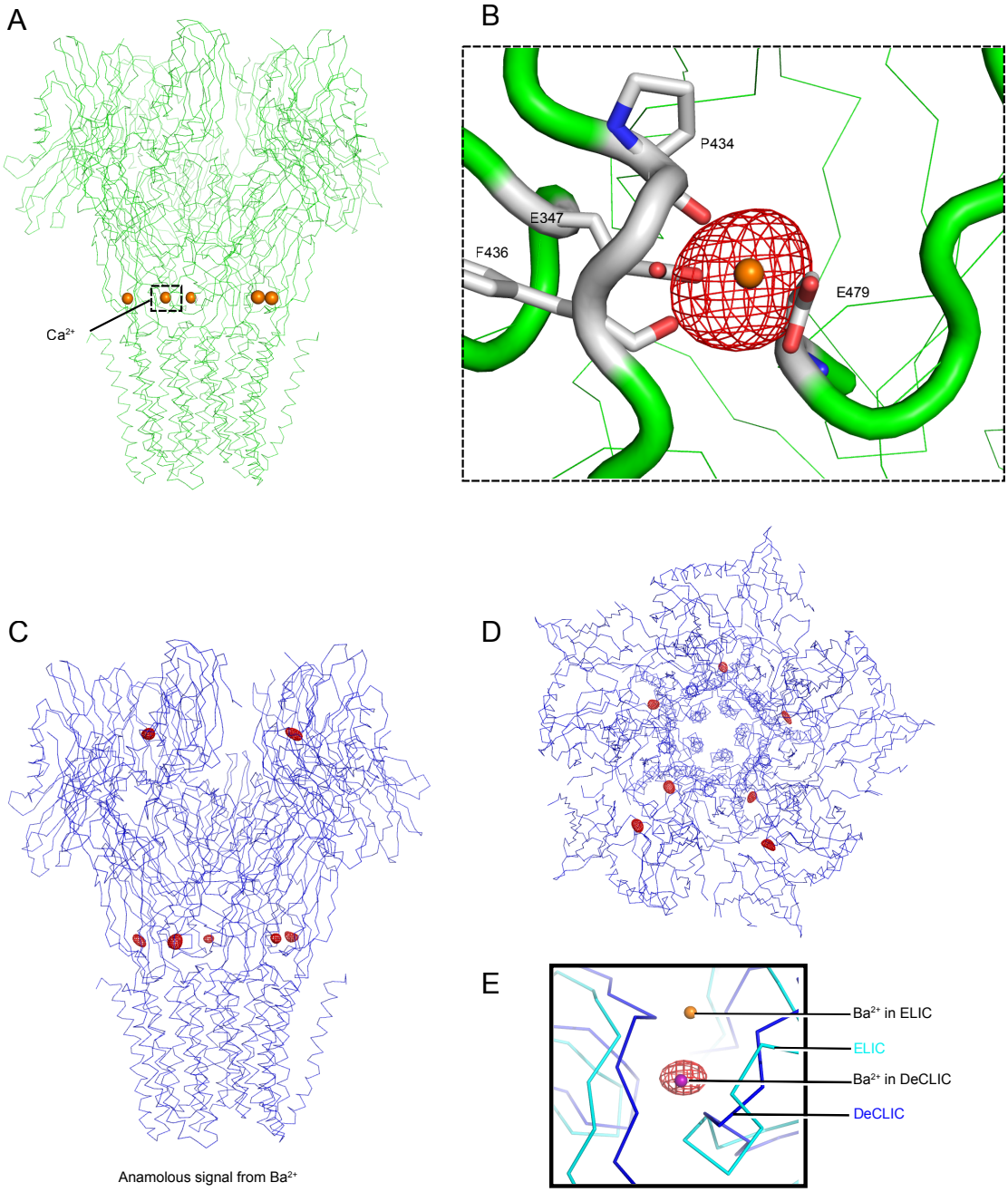


**Figure S9. Divalent cation sites in DeCLIC.**
(A) DeCLIC structure in the presence of $Ca^{2+}$, viewed from the membrane plane, with $Ca^{2+}$ ions as orange spheres. (B) Detail view of $Ca^{2+}$ contacts in the boxed region of *A*, with overlaid anomalous density of $Ba^{2+}$ (red mesh, contoured at 4 σ). (C) View as in a with overlaid Ba2+ anomalous signal as in *B*. (D) View as in c from the periplasmic side. (E) Superposition of $Ba^{2+}$-bound DeCLIC and ELIC structures (PDB ID 2YN6), showing $Ba^{2+}$-binding sites.

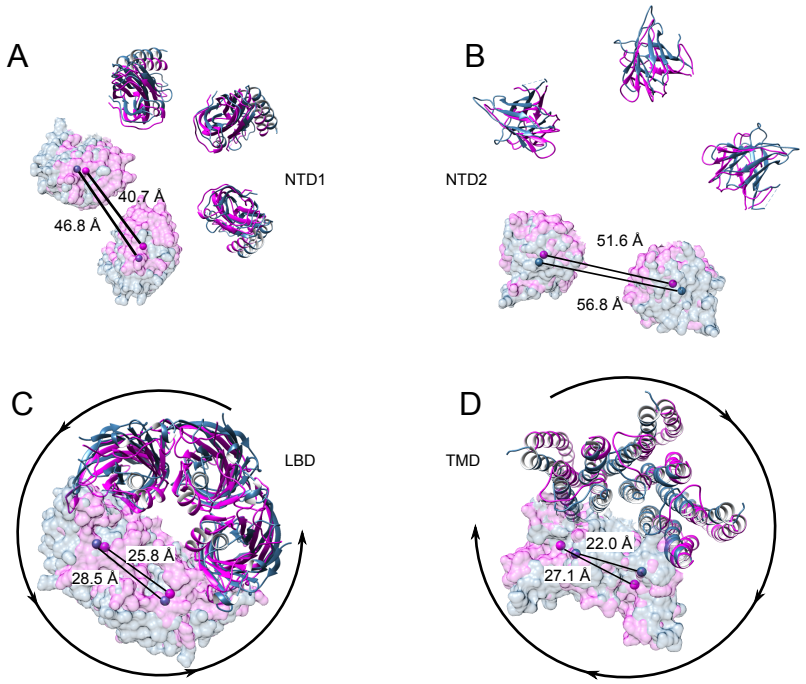


E

| Interface | Interface area (Å) |
|---|---|
| LBD-LBD (Channel Closed) | 789.4 |
| LBD-LBD (Channel Open) | 1069.0 |
| TMD-TMD (Channel Closed) | 1256.6 |
| TMD-TMD (Channel Open) | 248.2 |

**Figure S10. Quaternary structure transitions between $Ca^{2+}$ bound and $Ca^{2+}$ free DeCLIC.**

Panels (A)–(D) illustrate COM distances between adjacent DeCLIC subunits in the presence (blue) or absence (magenta) of $Ca^{2+}$, calculated separately at the level of *A*, the NTD1 lobes; (B) the NTD2 lobes; (C) the LBD; (D) the TMD. (E) Buried surface area ($Å^2$) at the subunit interface in each region illustrated in (A)–(D).

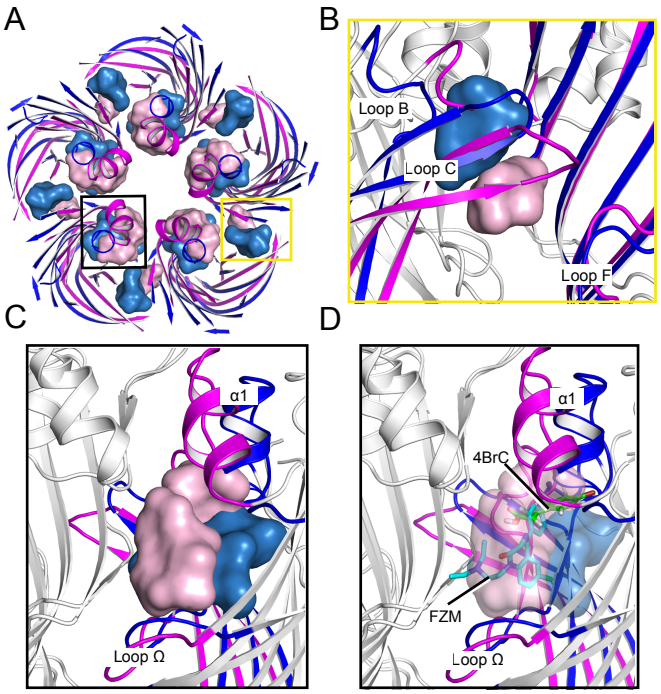


**Figure S11. Remodeling of cavities in the LBD.**
(A) Superposition of the DeCLIC LBD in the presence (blue) and absence (magenta) of $Ca^{2+}$, viewed from the periplasmic side, with cavities in orthosteric and vestibular sites calculated using Hollow[18]. (B) Detail view of the orthosteric-site cavity in the yellow-boxed region of *A*. (C) Detail view of the vestibular allosteric-site cavity in the black-boxed region of *A*. (D) View as in *C* showing the superimposed position of flurazepam (FZM, green) as co-crystallized with ELIC (PDB ID 2YOE), and of 4-bromo-cinnamate (4BrC, blue) as co-crystallized with sTeLIC (PDB ID 6FLI).

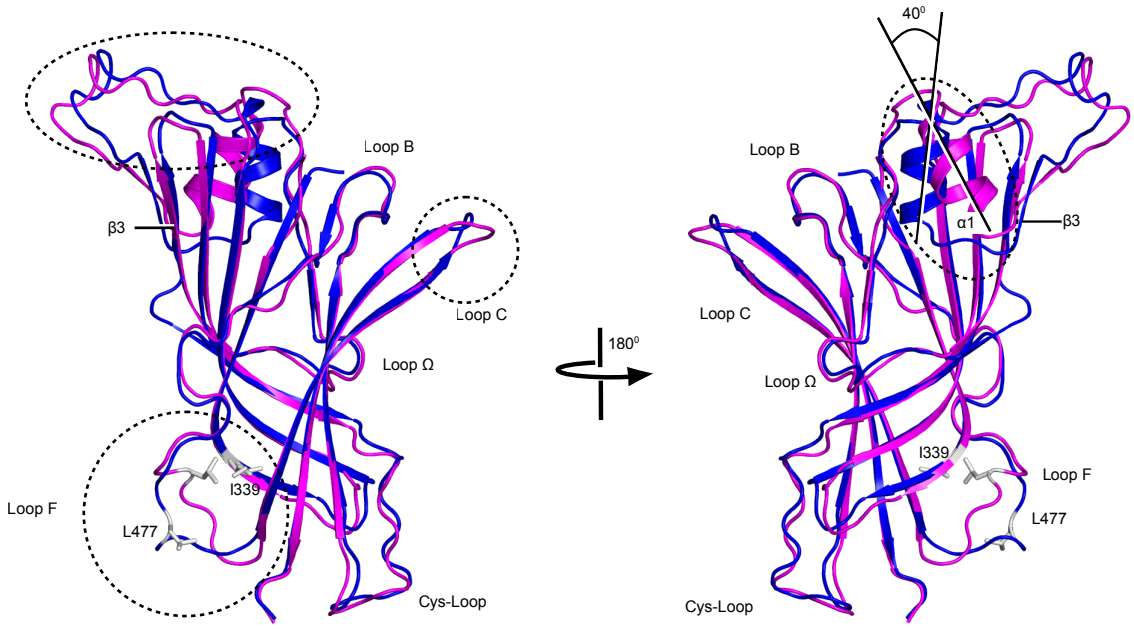


**Figure S12. Tertiary structure transitions in the LBD between $Ca^{2+}$ bound and $Ca^{2+}$ free DeCLIC.**
Superposition of a single LBD subunit of DeCLIC in the presence (blue) and absence (magenta) of $Ca^{2+}$, viewed perpendicular to the membrane plane from either the periplasmic space (left) or within the LBD vestibule (right).

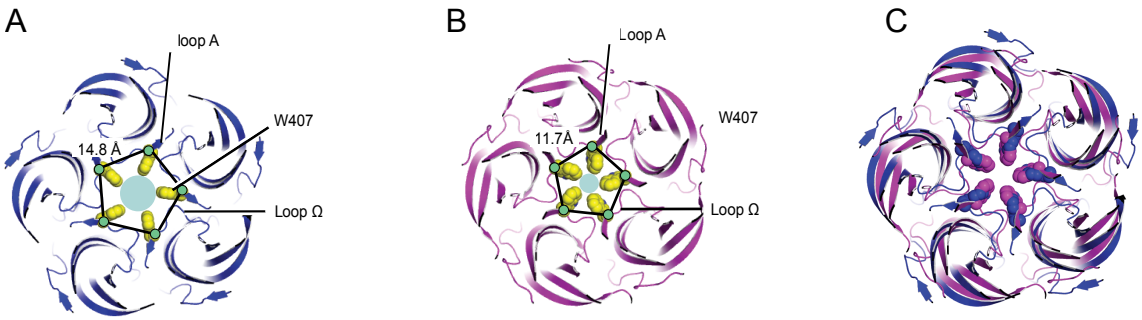


**Figure S13. Rearrangement of the vestibule constriction ring around loop Ω.** (A) The LBD in $Ca^{2+}$ bound (blue) conformation viewed from periplasmic side, showing residue W407 as spheres. (B)View as in a for the $Ca^{2+}$ free state. (C) Superposition of the LBD in $Ca^{2+}$ bound (blue) and $Ca^{2+}$ free (magenta) conformations.

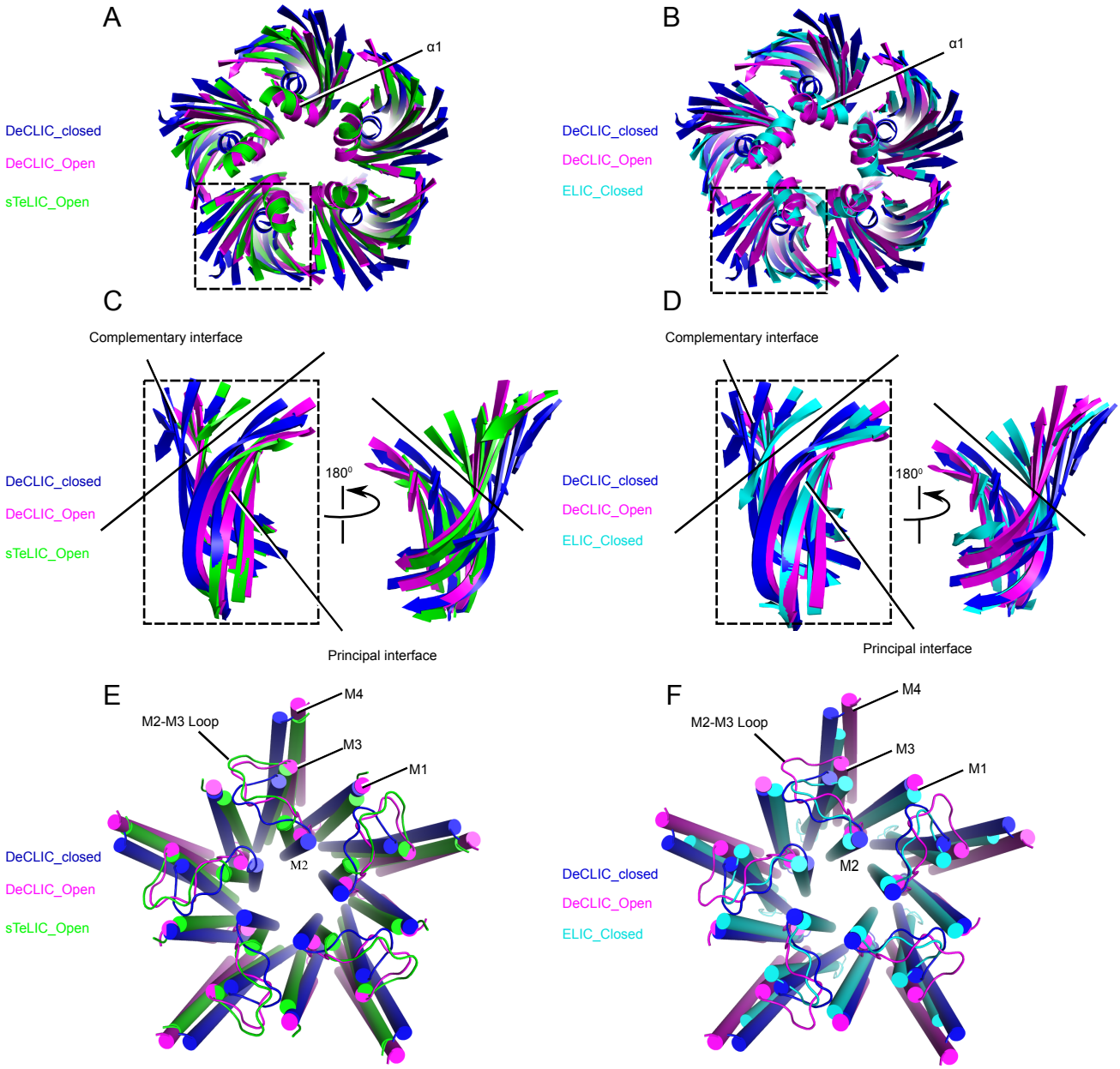


**Figure S14. State-dependent structural alignment among prokaryotic pLGICs.** (A) Superpositions of $Ca^{2+}$ bound DeCLIC (blue) with ELIC (PDB ID 6FL9) and sTeLIC (PDB ID 6FL9), viewed from the periplasmic side, with loops hidden for clarity. (B) Superposition as in a of $Ca^{2+}$ free DeCLIC (magenta). (C) Superposition as in *A* of the LBD of $Ca^{2+}$ bound DeCLIC (blue), viewed from the membrane plane. (D) Superposition as in c of the LBD of $Ca^{2+}$ free DeCLIC (magenta), showing alignment with both ELIC and sTeLIC in this domain. (E) Superposition as in *A* of the TMD of $Ca^{2+}$ bound DeCLIC (blue), viewed from the periplasm, showing alignment with ELIC. (F) Superposition as in *E* of the LBD of $Ca^{2+}$ free DeCLIC (magenta).

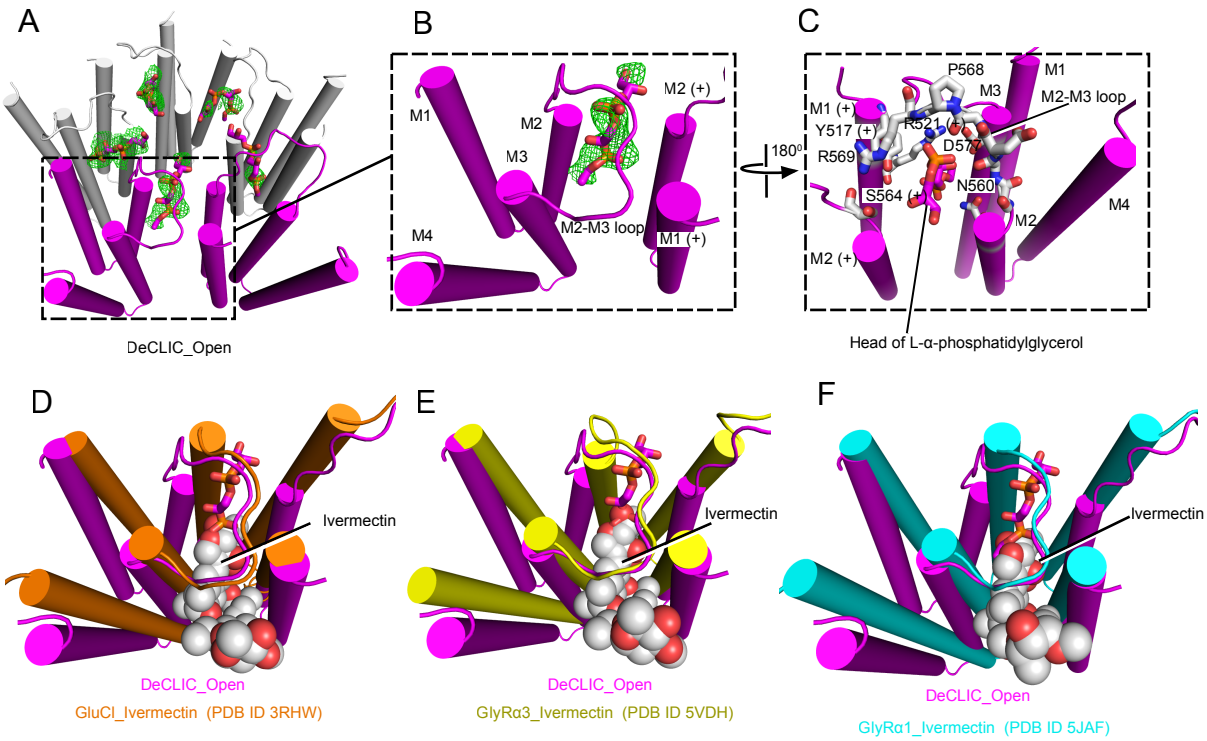


**Figure S15. Transmembrane lipid sites in $Ca^{2+}$ free DeCLIC.**
(A) View of two adjacent TMD subunits in the absence of $Ca^{2+}$ (magenta), with polar heads of L-α-phosphatidylglycerol molecules modeled as sticks. The Fo-Fc omit map (green) is overlaid and contoured at 2.5 σ. (B) Detail views of lipid contacts in the boxed regions of *A*. (C) Rotated view of the interaction between the lipid head and side-chains from the receptor, shown in ball-and-stick, especially R569, R521. (D)-(F), Structural pairwise comparison of the TMD allosteric modulation site in GluCl (D), GlyRα3 (E) and Glyα1 (F).

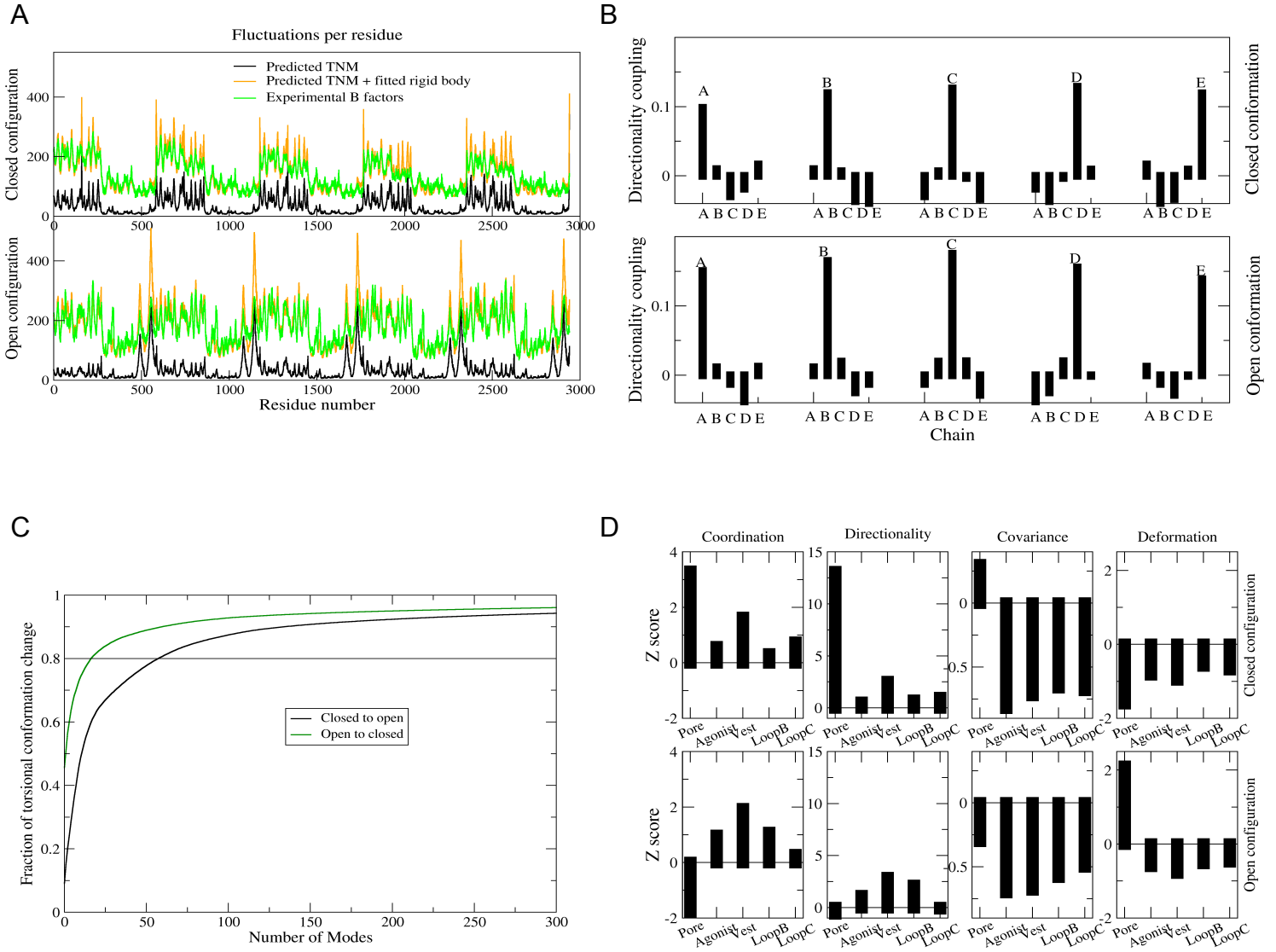


**Figure S16. Dynamical coupling of DeCLIC functional sites in the torsional network model.**
(A) Atomic fluctuations predicted with the TNM model (black), predicted fluctuations plus rigid body motions fitted with rescaled ridge regression (orange) and experimental B factors (green) for the closed and open conformation. The correlation coefficients between observed and fitted fluctuations are 0.94 for the closed and 0.88 for the open conformation.
(B) Fraction of the torsional part of the conformational change explained by normal modes, ranked by their contribution to the conformational change. Fewer modes, mostly of low frequency, are necessary to explain the open-to-closed transition (mode 4 alone explains 46% of this transition) than the reverse one.
(C) Co-directionality coupling between atoms in the same and in different chains. The largest couplings are exhibited by atoms in the same chain followed by atoms in neighbouring chains, while second neighbour chains have negative co-directionality.
(D) Z-scores of the dynamical couplings between atoms belonging to different functional sites in the closed (upper row) and the open conformation (lower row). The four columns depict the coordination, directionality, covariance and deformation couplings, respectively.

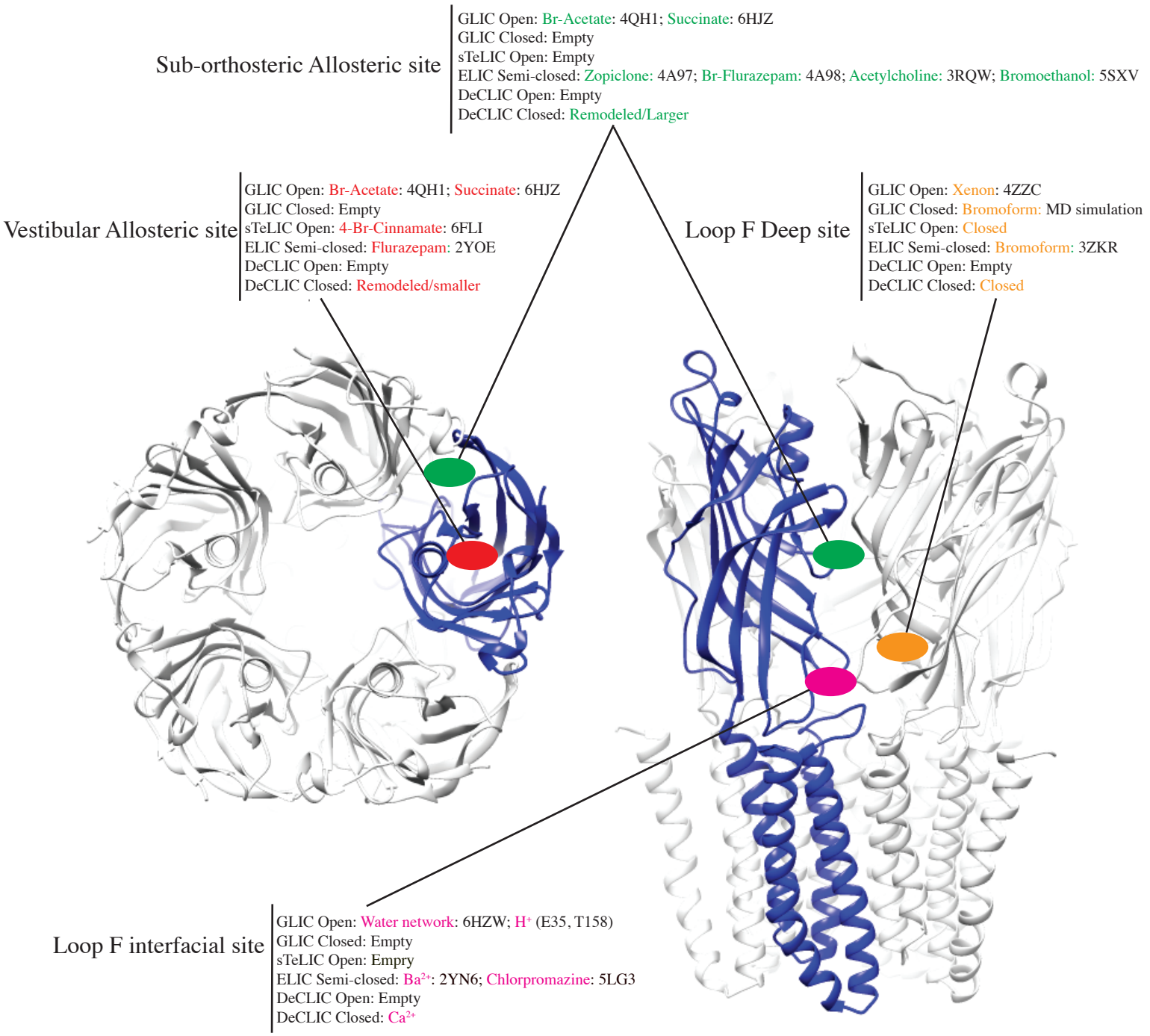


**Figure S17. Summary of known allosteric binding sites in the LBD of bacterial pLGICs.**

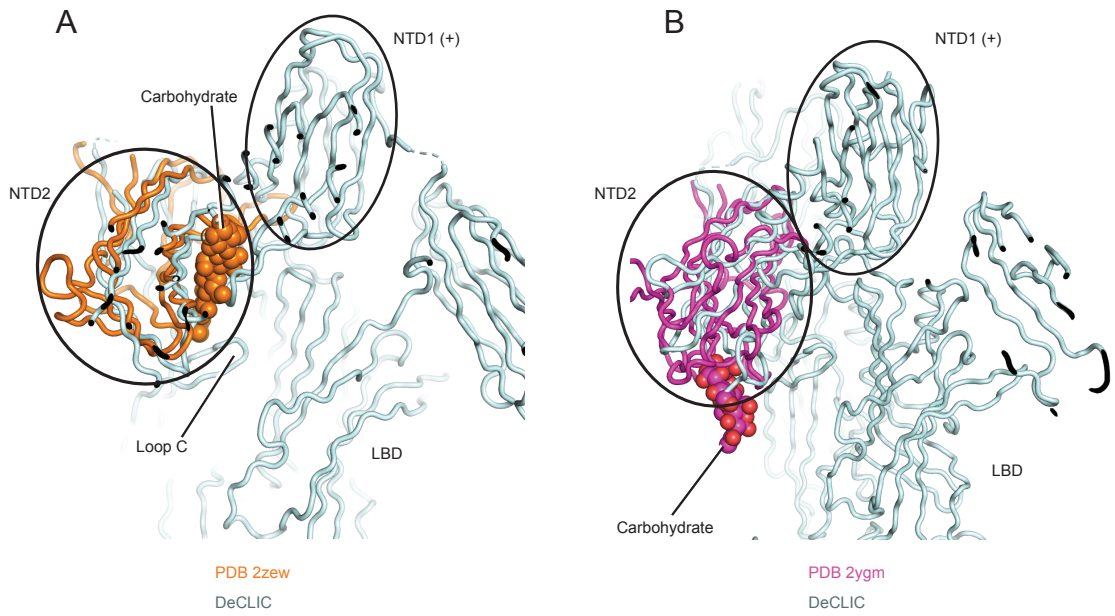


**Figure S18. The NTD shares a similar topology with two sugar-binding proteins.**

(A) Superposition of a sugar binding protein (orange; PDB ID 2ZEW) with NTD2; the carbohydrate is shown as CPK spheres. (B) Superposition of a second sugar binding protein (pink; PDB ID 2YGM) with NTD2, found with the Dali server; the carbohydrate is shown as CPK spheres.

**Table S1**

| | DeCLIC $Ca^{2+}$ bound Channel closed | DeCLIC Channel Open | DeCLIC NTD1 (34-202) | DeCLIC Se-Met NTD1 (34-202) |
|---|---|---|---|---|
| **Data collection** | | | | |
| Beamlines | Soleil-PX1 (12/06/2016) | Soleil-PX1 (08/07/2016) | Soleil-PX1 (13/04/2018) | Soleil-PX1 (13/04/2018) |
| Space group | P $2_12_12$ | P $2_1$ | P $6_1$ | P $6_1$ |
| Cell dimensions a, b, c (Å) α, β, γ (°) | 159.41, 337.25, 111.81 90.0, 90.0, 90.0 | 141.06, 116.03, 169.63 90.0, 109.17, 90.0 | 81.35, 81.35, 99.26 90.0, 90.0, 120.0 | 81.13, 81.13, 99.59 90.0, 90.0, 120.0 |
| Wavelength (Å) | 0.9786 | 0.9786 | 0.9786 | 0.9791 |
| Resolution (Å) | 48.18-**3.55** (3.64-3.55) | 48.61-**3.83** (3.93-3.83) | 40.75-**1.75** (1.79-1.75) | 40.63-**2-19** (2.25-2.19) |
| Anisotropy direction Resolution with CC1/2 > 0.3 | | | | |
| Overall (Å) | 3.55 | 3.83 | 1.75 | 2.19 |
| | along h axis (Å) 3.59 | along 0.93 a*-0.36c*(Å) **3.83** | along h axis (Å) **1.75** | along h axis (Å) **2.19** |
| | along k axis (Å) **3.55** | along k axis (Å) 5.41 | along k axis (Å) **1.75** | along k axis (Å) **2.19** |
| | along l axis (Å) 3.97 | along -0.01 a*+ 1.00 c*(Å) 4.17 | along l axis (Å) 1.80 | along l axis (Å) **2.19** |
| Reflections measured | 979185(64866) | 188272(12594) | 277462(19708) | 258775(16578) |
| Reflections unique | 73420(5125) | 49576(3486) | 37644(2724) | 19016(1317) |
| Completeness (%) | 99.6/95.4 | 99.3/94.6 | 99.8/97.9 | 99.9/94.7 |
| CC ½ (%) | 99.9(37.2) | 99.9(44.8) | 99.9(65.2) | 99.9(73.6) |
| *I/ σ(I)* | 11.0(0.7) | 7.6(0.6) | 16.4(1.2) | 13.6(12.6) |
| $R_{merge}$ | 0.17(3.64) | 0.08(1.57) | 0.06(1.21) | 0.12(0.99) |
| Multiplicity | 13.3(12.7) | 3.8(3.6) | 7.4(7.2) | 14.3(2.5) |
| **Refinement** | | | | |
| Resolution cut-off (Å) | 48.04-**3.55** | 25.00-**3.83** | 24.84-**1.75** | |
| Rfactor | 0.20 | 0.25 | 0.20 | |
| Rfree | 0.26 | 0.28 | 0.22 | |
| No. of protein atoms | 23260 | 23193 | 2428 | |
| B factor overall ($Å^2$) | 140.67 | 145.97 | 37.98 | |
| Ramachandran favored (%) | 93.55 | 93.54 | 95.25 | |
| Molprobity score | $99^{th}$ | 99th | 83rd | |
| PDB ID | 6V4S | 6V4A | 6V4B | |

Table S1. Diffraction data collection and model refinement statistics

**Table S2. Compounds tested without replicable effects on DeCLIC currents:**

***Sugar derivatives:***
Galactose
Glucose
Maltose
Sorbitol
Sucrose

***Salts:***
Sodium acetate
Ammonium chloride
Ammonium formate
Ammonium sulfate
Sodium citrate
Sodium gluconate
Sodium glycolate
Sodium sulfate

***Amino-acid derivatives:***
Benzamidine
Cysteamine
Ethylamine
GABA
GABOB
Glycine
Histamine
Serotonin
Taurine
ThiamineTyramine

***Lipidic compounds:***
4-Bromocinnamic acid
Bromoform
4-Bromophenethylamine
Cannabidiol
*N*-(*p*-Courmaroyl)-*L*-homoserine lactone
1,4-Dihydroxy-2-naphthoic acid
*n*-Dodecyl $\beta$-*D*-maltoside
Ethanol
Fipronil
Ivermectin
Picrotoxin
Propofol